IEEE Access
Multidisciplinary | Rapid Review | Open Access Journal

Received October 27, 2018, accepted November 19, 2018, date of publication November 30, 2018,
date of current version December 27, 2018.

Digital Object Identifier 10.1109/ACCESS.2018.2884225

Image-Based Visibility Estimation Algorithm for Intelligent Transportation Systems

LI YANG[1], (Student Member, IEEE), RADU MURESAN[2], (Member, IEEE), ARAFAT AL-DWEIK[1,3], (Senior Member, IEEE), AND LEONTIOS J. HADJILEONTIADIS[3], (Senior Member, IEEE)

[1]Department of Electrical and Computer Engineering, Western University, London, ON N6A 3K7, Canada
[2]School of Engineering, University of Guelph, Guelph, ON N1G 2W1, Canada
[3]Department of Electrical and Computer Engineering, Khalifa University, Abu Dhabi 127788, United Arab Emirates

Corresponding author: Arafat Al-Dweik (arafat.dweik@ku.ac.ae)

This work was supported in part by the Ministry of Transportation Ontario, Highway Infrastructure Innovation Funding Program (HIIFP) under Grant 051938 and in part by the ICT Fund, UAE, under Grant 11/15/TRAICTFund/KU.

ABSTRACT Posted road speed limits contribute to the safety of driving, yet when certain driving conditions occur, such as fog or severe darkness, they become less meaningful to the drivers. To overcome this limitation, there is a need for adaptive speed limits system to improve road safety under varying driving conditions. In that vein, a visibility range estimation algorithm for real-time adaptive speed limits control in intelligent transportation systems is proposed in this paper. The information required to specify the speed limit is captured via a road side unit that collects environmental data and captures road images, which are then analyzed locally or on the cloud. The proposed analysis is performed using two image processing algorithms, namely, the improved dark channel prior (DCP) and weighted image entropy (WIE), and the support vector machine (SVM) classifier is used to produce a visibility indicator in real-time. Results obtained from the analysis of various parts of highways in Canada, provided by the Ministry of Transportation of Ontario, show that the proposed technique can generate credible visibility indicators to motorists. The analytical results corroborated by extensive field measurements confirmed the advantage of the proposed system when compared to other visibility estimation methods such as the conventional DCP and WIE, where the proposed system results exhibit about 25% accuracy enhancement over the other considered techniques. Moreover, the proposed DCP is about 26% faster than the conventional DCP. The obtained promising results potentiate the integration of the proposed technique in real-life scenarios.

INDEX TERMS Visibility, machine learning, image processing, intelligent transportation system, smart cities, dark channel prior, entropy, SVM.

I. INTRODUCTION

A. PRELIMINARIES AND LITERATURE SURVEY

Transition from a city to a 'smart city' potentiates enhanced quality, performance and interactivity of urban services, in an effort to improve the quality of life in dense cities. Being a central part of smart cities, Intelligent Transportation Systems (ITSs) have been applied to numerous areas, including relieving traffic congestion, reducing traffic accidents, fuel consumption and pollution [1]– [4]. An ITS often collects data from a variety of sources including sensors and cameras, and analyses them to provide users with useful information.

Car accidents is a pressing issue in the modern society, with a large number of collisions occurring annually. Speeding is a dangerous driving behavior, especially on the highways, easily leading to serious accidents [5]. As such, speed limit control is a key element in ITSs, which is used to reduce the probability of making accidents by setting the speed limit to values that suit the road conditions. However, 73% of fatal accidents occur at low speeds of less than 55km/h [6], which is due to the fact that posted speed limits are optimized to the road conditions, but they often ignore the variable weather conditions. In order to improve road safety, speed limits should be based on both the road and weather conditions, and should be updated in real-time. Therefore, drivers become aware of the safe speed that they should travel at and could maintain an appropriate safety distance between cars [7]. Speed adjustment and safety distance maintenance can prevent traffic collisions and stop-and-go traffic behavior, which

may also reduce the emission of carbon dioxide and other global-warming gases [8]. Moreover, assigning the speed limits while considering the driving conditions enables tracking and estimating the driver's behavior more accurately [9], [10].

Two of the main factors that have a direct impact on driving speed are visibility and traffic congestion [11]. In limited visibility conditions, car accidents occur often because motorists cannot see objects at a sufficient distance that enables them to stop or slow based on the behavior of other leading vehicles [12]. A safe driving speed can be computed if we can monitor the visibility on the roads in real-time or quasi-real-time [13]. Thus, traffic accidents can be avoided if poor visibility alerts and safe driving speeds are conveyed to motorists in a timely manner.

Extreme weather conditions such as rain, snow, fog, dust, sand, smog or any combination of them make it difficult for the drivers to clearly see the road ahead of them [12]. Each of the weather conditions affects the visibility by a different level, and for a different time period. For example, snowy weather often results in poor visibility, especially during snowstorms [14]. Foggy weather conditions is a common trigger for lower visibility, therefore, intelligent fog detection and visibility estimation based on fog have been considered widely in the literature [15]– [17]. Darkness is another main source for limited visibility that is mostly faced during nighttime driving, particularly for roads with few or even no street lighting [17].

Generally speaking, measuring visibility accurately is difficult due to two main reasons [12]. First, the visibility can be affected by many parameters such as light sources and absorption, and hence, human-perceived visibility is difficult to estimate accurately. Second, visibility can be represented by a value only when the atmosphere is uniform, which seldom happens because weather conditions often change rapidly. Images and videos are typically the main sources to judge visibility, so cameras mounted on Road Side Units (RSU) and in-vehicle devices have been used to collect data to measure visibility as described in [16] and [18]. Huang [19] use on-board camera to collect images and estimate visibility. Furthermore, vehicle-to-infrastructure (V2I) communication can be used to connect the devices and perform analysis [20].

In the literature, image processing algorithms are often used to estimate visibility. Measuring the brightness and contrast of a target against a background are used to estimate the visibility as reported in [21]. In [14], gray scale levels are exacted from images to indicate visibility because they can reflect some information about visibility. High-pass filters including Gaussian high-pass filter and homomorphic filter are also used to measure atmospheric visibility [22]. Machine learning algorithms are used to estimate visibility as well, for example, Giyenko *et al.* [15] use a neural network approach for estimating visibility distances. Varjo and Hannuksela [23] propose support vector machine (SVM) approach to classify images and estimate the visibility. However, the accuracy of the aforementioned techniques is limited because of the wide range of conditions where visibility measurements are typically performed.

Haze removal algorithms are typically used to enhance the clarity of digital images [24]– [34]. In most of these algorithms, the thickness of the haze, or the fog density, can be obtained and used to indicate the visibility level in the image. However, fog density does not meticulously reflect the visibility in several cases such as the nighttime, and thus, such techniques cannot accurately detect the visibility level in various conditions [35].

B. MOTIVATION AND KEY CONTRIBUTIONS

Consequently, accurate image-based visibility estimation in general weather and time conditions requires extracting, analyzing and combining all visibility-related features that can be extracted from a particular image. Therefore, in this paper we capitalize on our work [36] and [37], and propose a new visibility algorithm for integration with the portable, low-power and low-cost Scalable Enhanced Road Side Units (SERSUs). The proposed visibility estimator is designed to extract and combine visibility indicators obtained using three main algorithms from image processing and machine learning. In particular, a fast version of the dark channel prior (DCP) algorithm [35], [38] is used to detect and calculate the current fog density from foggy images. The fog density is a very useful indicator for the visibility during the day time, and the fast implementation is desired for real-time systems with limited computational capabilities. Weighted Image Entropy (WIE) [39], [40] is further utilized to extract the gray scale distribution information in an image, which is then used to calculate the visibility level. The WIE can be efficiently used to identify day and night images, but it might be difficult to use it for identifying images with different levels of darkness. A second visibility indicator is obtained using a Support Vector Machine (SVM) classifier [23], [41], which is mostly designed based on human perception. The SVM performance depends on the number and type of training images, and hence, the results obtained using the SVM might be different from the true visibility perceived by humans. To overcome the limitations of the WIE and SVM when used individually, an enhanced visibility estimator is proposed by combining the WIE and SVM while the fog density is invoked to optimize the combining process. Extensive experiments were conducted to calibrate and validate the developed algorithm, and the results obtained show that the proposed algorithm outperforms other well established algorithms. Once the final visibility level is estimated, it can be used to adjust the speed limit for the current road accordingly.

C. PAPER ORGANIZATION

The rest of this paper is organized as follows. Section II describes some background information about the DCP, WIE and SVM. Section III presents the fast DCP and fog density estimation. Section IV describes the proposed WIE, SVM and the comprehensive visibility indicator based on real highway

images. Section V presents the experimental and numerical results, and finally the conclusion is presented in Section VI.

II. BACKGROUND

A. DARK CHANNEL PRIOR (DCP)

DCP can be effectively used for single image defogging as reported in [35]. In computer vision and computer graphics, the foggy image formation model can be described as [35],

$$\mathbf{I}(\mathbf{x}) = \mathbf{J}(\mathbf{x})t(\mathbf{x}) + \mathbf{A}(1 - t(\mathbf{x})) \tag{1}$$

where $\mathbf{I}(\mathbf{x})$ represents the foggy image that needs to be defogged, $\mathbf{J}(\mathbf{x})$ is the intrinsic non-foggy image, $\mathbf{A}$ is the global atmospheric light composition parameter, and $t(\mathbf{x})$ is the transmittance which describes the ratio of the light that reaches the camera to the whole light reflected from the object. In (1), $\mathbf{I}(\mathbf{x})$ is known and the goal is to find the original non-foggy image $\mathbf{J}(\mathbf{x})$. Therefore, $\mathbf{A}$ and $t(\mathbf{x})$ should to be determined according to (1) to compute $\mathbf{J}(\mathbf{x})$.

DCP is based on extensive observation and summarization on the non-sky region of foggy outdoor images. In most non-sky regions of images, some pixels always have very low values, at least in one color channel. Therefore,

$$J^{dark}(\mathbf{x}) = \min_{\mathbf{y}\in\Omega(\mathbf{x})} \left(\min_{c} J^{c}(\mathbf{y}) \right) \approx 0 \tag{2}$$

where, $c \in \{R, G, B\}$, and $\{R, G, B\}$ correspond to red, green and blue color channels, respectively. J^c and I^c are the color channels of $\mathbf{J}$ and $\mathbf{I}$, respectively. Assuming that $\Omega(\mathbf{x})$ is a local patch centered at **x,** also called the neighborhood area of the pixel $\mathbf{x}$, and the initial transmittance $t(\mathbf{x})$ in each patch $\Omega(\mathbf{x})$ is a constant, denoted as $\tilde{t}(\mathbf{x})$, after formula conversion [35], then,

$$\tilde{t}(\mathbf{x}) = 1 - \min_{\mathbf{y}\in\Omega(\mathbf{x})} \left(\min_{c} \frac{I^{c}(\mathbf{y})}{A^{c}} \right) \tag{3}$$

Consequently, $\tilde{t}(\mathbf{x})$ in (3) is an estimate of the transmittance.

According to DCP theory, in the dense fog area of a foggy image $\mathbf{I}$, the gray scale value of its dark channel image $\mathbf{J}^{dark}$ significantly increases. Each pixel $J^{dark}(x, y)$ in the dark channel image is the minimum pixel value in the neighborhood area of pixel (x, y) in the original image. As a consequence, the gray scale value can be used to indicate the fog density.

In the above-mentioned inferences, it is assumed that the value of global atmospheric light $\mathbf{A}$ is known. In practice, the value of $\mathbf{A}$ can be obtained from the foggy image by means of its dark channel image. The specific steps are [35]:

1) Extract the area represented by 0.1% of the brightest pixels from the dark channel image.
2) Find the value of the pixel with the maximum brightness in the area of 1), and use the pixel value on the corresponding position in the original foggy image $\mathbf{I}$ as the estimated value of $\mathbf{A}$, denoted as $\hat{\mathbf{A}}$.

Since the DCP uses a segmentation method in image processing, the initial transmission graph has some obvious blobs, resulting in poor preservation of the edges of the image. Therefore, He *et al.* [35] use the soft matting process proposed in [42] to obtain the optimal transmission graph $\tilde{t}(\mathbf{x})$. It is worth noting that when the value of the transmission graph $\tilde{t}(\mathbf{x})$ is very small, it makes the value of $\mathbf{J}(\mathbf{x})$ too large, and hence, the image is excessively transferred to the white field. Therefore, it is useful to set a minimum threshold value t_0 for $\tilde{t}(\mathbf{x})$. If the value of $\tilde{t}(\mathbf{x})$ is less than t_0, then $\tilde{t}(\mathbf{x}) = t_0$. The image after defogging can be derived by:

$$\tilde{\mathbf{J}} = \frac{\mathbf{I}(\mathbf{x}) - \hat{\mathbf{A}}}{\max(\tilde{t}(\mathbf{x}), t_0)} + \hat{\mathbf{A}} \tag{4}$$

where, $\tilde{\mathbf{J}}$ is the image after defogging, $\mathbf{I}$ is the foggy image and t_0 is a constant coefficient to reduce the image noise.

In the solving process of DCP algorithm, the neighborhood minimum value of each pixel of the image is needed, and the computational complexity increases non-linearly with the neighborhood area size. In addition, the soft matting process needs to construct the Matting Laplacian matrix whose size is the height of the image multiplied by its width. Therefore, the spatial and time complexity of the algorithm increases drastically, as the number of pixels in the image increases. The algorithm is time-consuming and has high computational complexity, which makes it difficult to be used in real-life applications. These issues are addressed in the proposed improvements described in Section III-A.

B. WEIGHTED IMAGE ENTROPY (WIE)

The image entropy is expressed as the average number of bits in the gray scale sets of the image [39], and its unit is bit/pixel, which reflects the average amount of information in the image. The one-dimensional entropy of an image represents the amount of information contained in the aggregate feature of the gray scale distribution in the image. Let P_i represent the proportion of pixels with the gray scale value i in the whole image. Then,

$$P_i = \frac{N(i)}{h \times w} \tag{5}$$

where $N(i)$ represents the number of pixels with the gray scale value i, h and w are the height and width of the image in pixels, respectively. As a result, P_i is also the probability that a specific gray scale value appears in the image and can be obtained from a gray scale histogram. Therefore, the image entropy for a 256 levels gray scale image can be calculated as

$$S = -\sum_{i=0}^{255} P_i \ln(P_i). \tag{6}$$

In the extreme case where the image is completely dark, then $P_0 = 1$, $P_i = 0 \; \forall \; i > 0$, and $S = 0$. For the other extreme case where the image is completely white (very foggy), then $P_{255} = 1$, $P_i = 0 \; \forall \; i < 255$, and $S = 0$. The upper bound on S can be achieved in the unlikely case where $P_i = 1/256 \; \forall \; i$, which results in the maximum possible entropy of $S = 5.5452$. Furthermore, if the importance of different pixel values is taken into consideration, then the information

entropy can be replaced by the weighted entropy S_W [39], which can be written as

$$S_W = -\sum_{i=0}^{255} \omega_i P_i \ln(P_i) \tag{7}$$

where ω_i is the weight assigned to the ith pixel value.

C. SUPPORT VECTOR MACHINE (SVM)

Support Vector Machine [41] technique is a supervised learning model related to learning algorithms, which can analyze data, identify patterns, classify and perform regression analysis.

SVMs are based on linear separation, but not all data can be linearly separated. For instance, two sets of points in a two-dimensional space may require a curve instead of a straight line to separate their boundaries. The principle of SVM is to map the points from low-dimensional space into high-dimensional space, making them linearly separable; and then use the principle of linear division to judge the classification boundary.

The linearly separable binary classification problem is to separate the original data by a straight line if the data points are only in a two dimensional or a hyperplane for multidimensional space. The largest interval method is used in SVM technique and it aims at finding the classification plane that results in largest classification boundary interval. The classification boundary is the value that shifts from the classification plane towards the points in two categories until the first data point is encountered. The distance between the classification boundaries of two categories is the classification interval.

The classification plane is expressed as $(\mathbf{w} \cdot \mathbf{x}) + b = 0$, where $\mathbf{w}$ is a normal vector that serves as the slope and b is the intercept. Note that $\mathbf{x}$ is a multidimensional vector and $(\cdot)$ represents the dot product of two vectors. The reciprocal of the sorting interval is $0.5\|\mathbf{w}\|^2$, so the optimization problem is expressed as

$$\begin{cases} \min_{w,b} \ \frac{1}{2}\|\mathbf{w}\|^2 \\ s.t.\ y_i((\mathbf{w} \cdot \mathbf{x}_i) + b + 1)) \geq 1, \ i = 1, \ldots, l \end{cases} \tag{8}$$

where, $\|.\|$ is the 2-norm of a vector and there are l points in total. The constraint in (8) is that the distance between each data point (x_i, y_i) and the classification plane is greater than or equal to 1. Among them, y_i is the classification of data.

Based on the above theory, a linear support vector classifier is proposed in [41], which after formula simplification can be expressed as,

$$\begin{cases} \mathbf{w}^* = \sum_{i=1}^{l} y_i a_i^* \mathbf{x}_i, \\ b^* = \frac{1}{j} \sum_{i=1}^{j} b_j^*, \quad b_j^* = y_j - \sum_{i=1}^{l} y_i \alpha_i (\mathbf{x}_i \cdot \mathbf{x}_j). \end{cases} \tag{9}$$

SVM is typically used for two-class classification problems, but the most common are the multi-classification problems. To apply SVM to multi-class classification, the one-versus-rest approach proposed in [43] is used in this work. The principle is to establish a SVM that separates one class from all other classes. For example, if there are M classes of training data, then we need to establish M support vector machines. When identifying $\mathbf{x}$ classification, we select the largest category of $g^c(\mathbf{x})$,

$$\begin{cases} f^c(\mathbf{x}) = \mathrm{sgn}(g^c(\mathbf{x})), \quad c \in [1, M] \\ g^c(\mathbf{x}) = \sum_{i=1}^{l} a_i^c y_i K(\mathbf{x}, \mathbf{x}_i) + b^c \end{cases} \tag{10}$$

where, $K(\cdot, \cdot)$ is the kernel function, which is used to define the mapping to transfer the low-dimensional problem into the high-dimensional problem, or calculate the difference between the two largest g as the confidence interval. If $\Delta g > 0$, then select the largest class of g to be the solution class c; otherwise, refuse to classify.

III. FOG DENSITY VISIBILITY INDICATOR BASED ON IMPROVED DARK CHANNEL PRIOR

As it can be noted from [35], the most time-consuming part of DCP algorithm is the dark channel image acquisition and soft matting process. Therefore, the key to improve the DCP algorithm and implement a fast DCP (fDCP) algorithm is to optimize these two parts. Towards this end, a new fast dark channel image acquisition and soft matting processes are proposed.

A. FAST DCP (FDCP)

1) FAST DARK CHANNEL IMAGE ACQUISITION ALGORITHM BASED ON BI-DIRECTIONAL TRAVERSAL

For each pixel (x, y) of the foggy image $\mathbf{I}$, find the pixel with minimum value in its neighborhood within a radius value r. Then, the dark channel image $\mathbf{D}$ is generated after traversing all pixels. This process is represented by

$$D(x_0, y_0) = \min_{\substack{x_0 - r \leq x \leq x_0 + r \\ y_0 - r \leq y \leq y_0 + r}} I(x, y). \tag{11}$$

As can be seen from (11), for each pixel of the foggy image $\mathbf{I}$, it is necessary to traverse each pixel of its r neighborhood. For a $m \times n$ image, after ignoring the regions near the edge, a process of finding the dark channel image needs to traverse about P_1 pixels, where

$$P_1 = (2r + 1)^2 \times m \times n. \tag{12}$$

Therefore, the number of traversals P_1 increases by increasing r. In practical applications, if the neighborhood radius $r = 10$ [35], then there are r pixel values and 21×21 pixel blocks around each pixel, and thus, $P_1 = 441 \times m \times n$. Consequently, the algorithm has a high computational complexity of $O(m \times n)$.

The proposed fDCP image acquisition algorithm is based on bidirectional traversal, which significantly reduces the redundancy of the traditional algorithm. This algorithm traverses the foggy image both, horizontally and vertically. In the horizontal traversal, for a certain pixel $(x_0 - 1, y_0)$, let the minimum pixel value of its horizontal r neighborhood be $D_X(x_0 - 1, y_0)$. Therefore, for the pixel (x_0, y_0), the minimum

pixel value of its horizontal r neighborhood $D_X(x_0, y_0)$ is determined by whether $D_X(x_0-1, y_0)$ equals $I(x_0-r-1, y_0)$:

Case 1: If $D_X(x_0-1, y_0) < I(x_0-r-1, y_0)$, the range of the position of the minimum value is $x_0-r \le x \le x_0+r-1$, so for pixel (x_0, y_0), it is only necessary to compare $D_X(x_0-1, y_0)$ with $I(x_0+r, y_0)$.

Case 2: If $D_X(x_0-1, y_0) = I(x_0-r-1, y_0)$, the algorithm needs to re-traverse the interval $x_0-r \le x \le x_0+r$. The formula to compute $D_X(x_0, y_0)$ is given in (13) at the bottom of the next page, where, $\mathbf{D}_X$ is the horizontal dark channel image and $\mathbf{I}$ is a foggy image. Traverse the image $\mathbf{I}$, using (13) to get the horizontal traversal image $\mathbf{D}_X$.

Next, the horizontal traversal image $\mathbf{D}_X$ is traversed vertically in a similar way, so the minimum pixel value $D_Y(x_0, y_0)$ of the vertical r neighborhood of a pixel (x_0, y_0) is given by (14) at the bottom of the next page where, $\mathbf{D}_Y$ is also the final dark channel image $\mathbf{D}$ after the horizontal and vertical traversals. If the edge regions are ignored, the fast dark channel image algorithm based on bidirectional traversal only needs to traverse the image at least P_2 times:

$$P_2 = 4 \times m \times n. \tag{15}$$

Moreover, the amount of calculation of P_2 is independent of r. In practical applications, if $r = 10$, the amount of calculations for P_2 is only 0.9% of P_1, and the calculation speed of this part is increased by at most 100 times, which reduces the overall execution time.

2) FAST SOFT MATTING USING THE INTEGRATION DIAGRAM

The soft matting algorithm requires a procedure which contains 10 times the operations to find the mean image and this procedure needs to be executed repeatedly, so the total number of operations would be large. The number 10 is determined according to our code, which shows that the function is invoked 10 times in each iteration, and this is the main time-consuming part of the soft matting algorithm. The conventional mean image is obtained by performing the following operations on each pixel (x, y) of the fog image $\mathbf{I}$,

$$\mathbb{E}(x, y) = \frac{1}{(2r+1)^2} \sum_{x=x_0-r}^{x_0+r} \sum_{y=y_0-r}^{y_0+r} I(x, y) \tag{16}$$

where, $\mathbb{E}(\cdot)$ denotes the mean value. Therefore, for an image that has $m \times n$ pixels, the process of mean calculation requires $(2r+1)^2 \times m \times n$ addition operations and $m \times n$ division operations. For a soft matting algorithm procedure involving 10 times mean image calculations, $(2r+1)^2 \times m \times n \times 10$ addition operations and $m \times n \times 10$ division operations will be required.

In this paper, the algorithm of integration diagram [44] is used to optimize the soft matting algorithm. First, this algorithm calculates the horizontal integration diagram of image $\mathbf{I}$. For a pixel (x, y), the integration diagram of the image $\mathbf{I}$ can be performed as,

$$C(x, y) = I(x, y) + C(x-1, y) + C(x, y-1) - C(x-1, y-1). \tag{17}$$

Through the integration diagram $\mathbf{C}$, the mean image can easily be obtained by,

$$\begin{aligned}\mathbb{E}(x, y) &= \frac{1}{(2r+1)^2}(C(x+r, y+r) + C(x-r-1, y-r-1) \\ &\quad - C(x-r-1, y+r) - C(x+r, y-r-1)).\end{aligned} \tag{18}$$

The method of using the integration diagram to compute the mean image requires approximately $6 \times m \times n$ addition or subtraction operations and $m \times n$ division operations. Since each division operation uses the same constant $(2r+1)^2$, on one hand we can use the multiplication operations to save time; on the other hand, we can combine the 10 times mean calculations in the soft matting algorithm and only perform $m \times n$ multiplication operations on the final result. Therefore, an operation of fast soft matting algorithm requires only $60 \times m \times n$ addition or subtraction operations and $m \times n$ multiplication operations, which greatly reduces the computational complexity of the algorithm.

B. FAST DEFOG ALGORITHM IMPLEMENTATION

Using the algorithms proposed in Sections II-A and III-A, the final fast defog algorithm can be described as follows:

1) Load the original image, an example is given in Fig. 1a.
2) Use the fast dark channel image acquisition algorithm based on bidirectional traversal to obtain the dark channel image $\mathbf{J}^{dark}$, Fig. 1b.
3) Obtain the atmospheric light composition: Get the 0.1% lightest pixels from the dark channel image, then find the pixel with the greatest brightness level among these pixels in the original foggy image as the value of $\hat{\mathbf{A}}$, which has three components, A_R, A_G, and A_B.
4) Generate the transmission graph using (3), Fig. 1c.
5) Use the fast soft matting method by the integration diagram to obtain a more accurate transmittance graph, Fig. 1d.
6) Adjust the original image according to the transmittance diagram and (3), and generate the defogged image, Fig. 2.

C. FOG DENSITY CALCULATION

By analyzing the more accurate transmittance graph in Fig. 1d, it can be noted that the brighter the area, the smaller the fog density. On the contrary, the darker the area, the greater the fog density. As a result, the fog density is inversely proportional to transmittance $t(\mathbf{x})$ and it can be estimated from the transmittance graph. In addition, the pixel values difference between the original and the defogged image is proportional to the fog density. By traversing each pixel of the original image and the transmittance graph, the difference can be represented by,

$$\Delta_{ij} = \max\left(\left|R_{i,j} - R'_{i,j}\right|, \left|G_{i,j} - G'_{i,j}\right|, \left|B_{i,j} - B'_{i,j}\right|\right) \tag{19}$$

where $(R_{i,j}, G_{i,j}, B_{i,j})$ and $(R'_{i,j}, G'_{i,j}, B'_{i,j})$ are the R, G, B components of pixel (i, j) in the original foggy and defogged

images, respectively. Then, the fog density $\mathcal{H}_{i,j}$ of the pixel (i, j) can be determined as,

$$\mathcal{H}_{i,j} = \left(\frac{1}{t_{i,j}} - 1\right) \Delta_{i,j} \tag{20}$$

where $t_{i,j}$ is the transmittance value of pixel (i, j) in the transmittance graph, an example is given in Fig. 1d, and $\Delta_{i,j}$ is the pixel value difference between the original and the defogged image (20). Eventually, the fog density of the image is the average of the fog density of all effective pixels,

$$F_D = \bar{\mathcal{H}} = \mathbb{E}\left(\mathcal{H}_{i,j}\right). \tag{21}$$

By noting that in most cases $0 \lesssim F_D \lesssim 0.5$, the normalized F_D can be defined as $\bar{F}_D = 2 \times 10^2$, and visibility using $\bar{F}_D$ can be defined as

$$V_1 = \left(100 - \bar{F}_D\right) \Pi\left(0, 100\right) \tag{22}$$

where $\Pi\left(a, b\right) \triangleq [\Phi\left(a\right) - \Phi(b)]$, and $\Phi\left(\cdot\right)$ is the unit step function.

Although F_D might be used to estimate the visibility, it does not generally produce accurate results because the DCP algorithm does not consider the visibility in other driving conditions such as night time. For example, the value of F_D for night images without fog will be relatively low, indicating good visibility. However, the visibility at night is actually limited due to the impact of darkness. Consequently, it is necessary to use more accurate techniques to analyze the visibility such that all conditions are covered.

IV. PROPOSED VISIBILITY METHODOLOGY

This section describes the proposed visibility estimation process where two initial visibility indicators are obtained using the WIE and SVM algorithms. Then, the results of the two algorithms are combined with the aid of the fog density estimated using the fDCP. The obtained visibility results are calibrated to span the range [0, 100], where the lower limit corresponds to the worst possible visibility. The visibility range can be converted to levels and distance in meters has hinted in Section V.

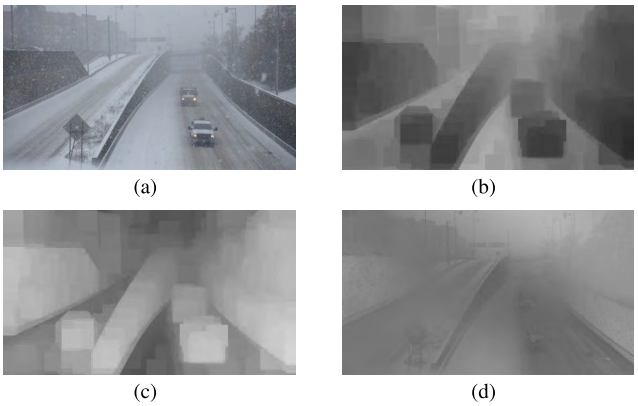

FIGURE 1. The images of DCP algorithm. (a) The original image. (b) The dark channel image. (c) The transmittance graph. (d) The more accurate transmittance graph.

FIGURE 2. The defogged image.

A. IMAGE-BASED VISIBILITY ESTIMATION USING THE WEIGHTED ENTROPY

As described in II-B, the image entropy reflects the richness of the information in the image as well as the clarity of the image. For example, histogram analysis is shown on the right-hand side of Fig. 3 for daytime, evening, midnight, and foggy images, respectively. The horizontal axis represents the pixel values ranging from 0 to 255 and the vertical axis represents the pixels' frequencies. Analyzing the histogram in Fig. 3a, which corresponds to a clear daytime image with high visibility, shows that a large number of pixels are located

$$D_X\left(x_0, y_0\right) = \begin{cases} \min\left(D_X\left(x_0 - 1, y_0\right), I(x_0 + r, y_0)\right), & D_X\left(x_0 - 1, y_0\right) < I\left(x_0 - r - 1, y_0\right) \\ \min\limits_{x_0 - r \le x \le x_0 + r} I(x_0, y_0), & D_X\left(x_0 - 1, y_0\right) = I\left(x_0 - r - 1, y_0\right) \end{cases} \tag{13}$$

$$D_Y\left(x_0, y_0\right) = \begin{cases} \min\left(D_Y\left(x_0, y_0 - 1\right), D_X\left(x_0, y_0 + r\right)\right), & D_Y\left(x_0, y_0 - 1\right) < D_X\left(x_0, y_0 - r - 1\right) \\ \min\limits_{y_0 - r \le y \le y_0 + r} D_X\left(x_0, y_0\right), & D_Y\left(x_0, y_0 - 1\right) = D_X\left(x_0, y_0 - r - 1\right) \end{cases} \tag{14}$$

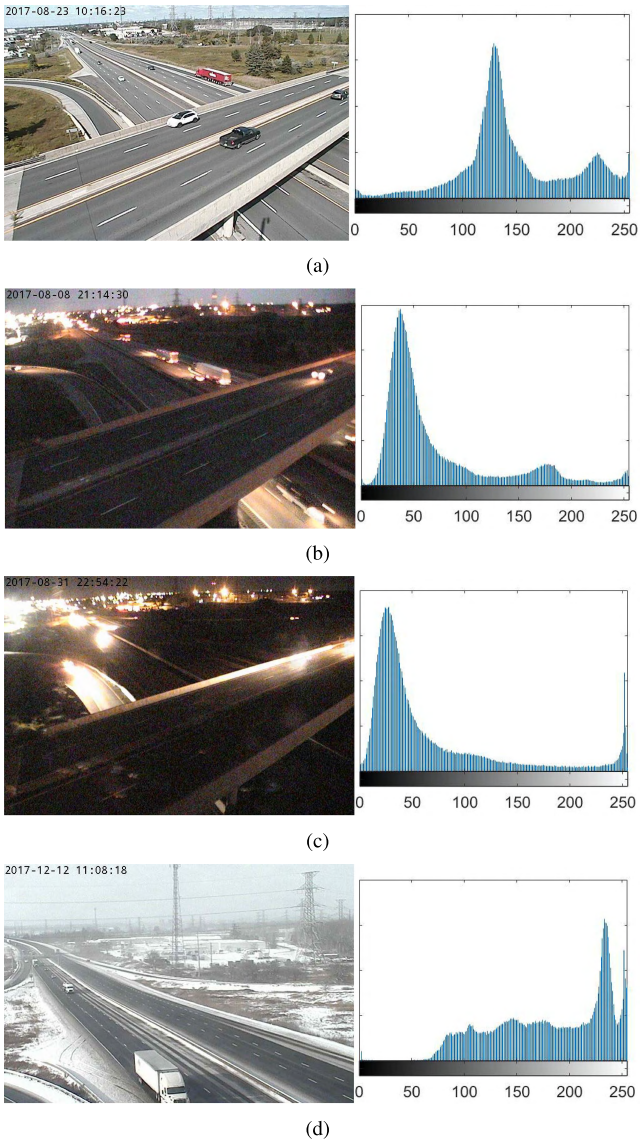

FIGURE 3. The grayscale histograms of images in different visibility conditions (daytime, evening, midnight, foggy).

at the center of the histogram while the remaining pixels are relatively uniformly distributed. As the darkness reduces the probability of high value pixels, the histograms of the evening and midnight images given in Fig. 3b and Fig. 3c respectively, show that their peaks are gradually shifted to the left, and they become more concentrated. On the contrary, the histogram of the foggy image with poor visibility shown in Fig. 3d has the pixels mainly clustered on the right side of the histogram, and are also very dense. Therefore, entropy-based image histogram analysis can be used to estimate the visibility level in a given image. However, additional processing is required to convert the entropy into a reliable visibility measure.

To develop a visibility indicator based on images' histograms, the concept of image entropy can be used where absolutely dark and foggy images give $S = 0$, and extremely clear images should give $S = 5.545$. However, these are ideal

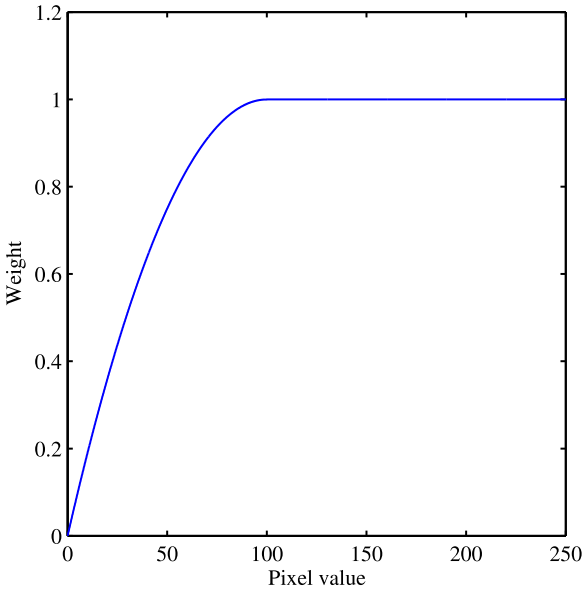

FIGURE 4. The weighting function graph.

scenarios that do not occur frequently in practical scenarios. For example, the entropies of Fig. 3a, 3b, 3c and 3d are 5.12, 4.84, 4.85 and 5.08, respectively. Therefore, it can be noted that the entropies of all images are relatively close to each other, which is due to the fact that S actually depends only on P_i rather than the pixel value itself, i.e., the entropy depends on the distribution of P_i rather than the order. Therefore, using weighted entropy (7) can give significant change in the entropies for different scenarios. For the dark images in Fig. 3b and Fig. 3c, the large number of pixels with low values correspond to low visibility conditions, and hence should be suppressed by assigning low weights to such pixels. Extensive experimental evaluation showed that the following weighting function gives good performance,

$$\omega_i = 10^{-4} i\,(200 - i), \quad 0 \le i \le 100. \tag{23}$$

As can be noted from (23), $\omega_0 = 0$ and $\omega_{100} = 1$.

In the case of high pixel values, the problem is different because foggy and clear daytime images have significant part of their pixels at upper range of the histogram, and thus, the weighting factors for such pixels are set to unity,

$$\omega_i = 1, \quad 100 < i < 255. \tag{24}$$

Consequently, other approaches should be used to estimate the visibility in such scenarios. The weighting function is depicted in Fig. 4, and the weighted entropies of Fig. 3a, 3b, 3c and 3d are 4.27, 1.25, 1.16, and 4.54, respectively. Therefore, it is apparent that the weighting process managed to give very low S_W values for the low visibility images. Moreover, it is more convenient to express the visibility using a normalized [0, 100] scale. Although theoretically $S_W \le 5.545$, testing a large number of images show that practically $S_W \lesssim 5$, which is due to the correlation of adjacent

pixels of any image. Therefore, the normalized S_W can be defined as $\bar{S}_W = 20 S_W \Pi(a, b)$.

As can be noted from S_W values, daytime foggy images can be misleading for the weighted entropy approach. Therefore, it is critical to use additional information from the image to tune S_W such that it provides more accurate results. As such, the fog density indicator F_D is a key tool that can be used to identify foggy daytime images. In this work, if $\bar{F}_D \leq 40$, then the image corresponds to daytime without or with little fog, otherwise it is a foggy image. Consequently, the value of $\bar{S}_W$ can be modified according to $\bar{F}_D$. **Algorithm 1** summarizes the computation of the visibility using the weighted entropy and fog density information, which is denoted as V_2.

Algorithm 1 Visibility Estimation Using Weighted Entropy

1: Convert colored image into gray scale
2: Compute F_D and $\bar{F}_D$
3: Calculate the gray scale histogram **H**
4: Compute S_W using (7), (23) and (24)
5: Compute $\bar{S}_W$
6: **If** $\bar{S}_W < 50$
7: $V_2 = \bar{S}_W$
8: **Elseif** $\left[\bar{S}_W \geq 50\right]$ & $\left[\bar{F}_D \leq 40\right]$
9: $V_2 = \bar{S}_W \left(1 + \left(\frac{\bar{F}_D}{\bar{S}_W}\right)^2\right)$
10: **Elseif** $\left[\bar{S}_W \geq 50\right]$ & $\left[\bar{F}_D > 40\right]$
11: $V_2 = \bar{S}_W \left(1 - \left(\frac{\bar{F}_D}{\bar{S}_W}\right)^2\right)$
12: **End**
13: **END**

It is worth noting that the ranges of $\bar{F}_D$ and the formulae used to calculate V_2 are optimized empirically based on a large set of images that correspond to different weather and lighting conditions.

Although WIE is an effective method to characterize the visibility, which is reflected clearly by the gray scale histogram as depicted in Fig. 3, there are several foggy images that produce quasi-uniform histograms, which couldn't be distinguished by the WIE. Consequently, the visibility estimates may not be accurate. In order to optimize the results, machine learning is invoked to perform image classification, where Support Vector Machines (SVM) is used, as described in the next subsection.

B. ESTIMATION OF IMAGE VISIBILITY BASED ON SVM ALGORITHM

Estimation of image visibility based on SVM can be considered as an image classification problem, where an image classifier is obtained through training with SVM algorithm to classify the images according to their visibility level. According to the theoretical analysis outlined in Section II-C, linear support vector classifier with the method One-Versus-Rest and (10) are used for multi-class classification. To train the SVM classifier, 1000 ground truth images are used, which are divided into six categories such that category 1 corresponds to low visibility conditions, midnight and thick fog images, while category 6 corresponds to daytime non-foggy images with high visibility. Six sample images each of which from different category are shown in Fig. 5. The image labeling process was performed with the help of three assessors, who were trained using a set of reference images from all categories. The reference images were classified based on the practical measurement procedure described in Section V. The final decisions for each image is made using the majority voting rule. Due to the relatively small number of images in the library, the training time was about four seconds using a 2.5 GHz Cote i7 processor with 8 GB RAM. The features vector applied to the classifier is the gray scale histogram **H,** and the training algorithm is presented as **Algorithm 2.** The classification result is denoted as $\Omega \in \{1, 2, ..., 6\}$.

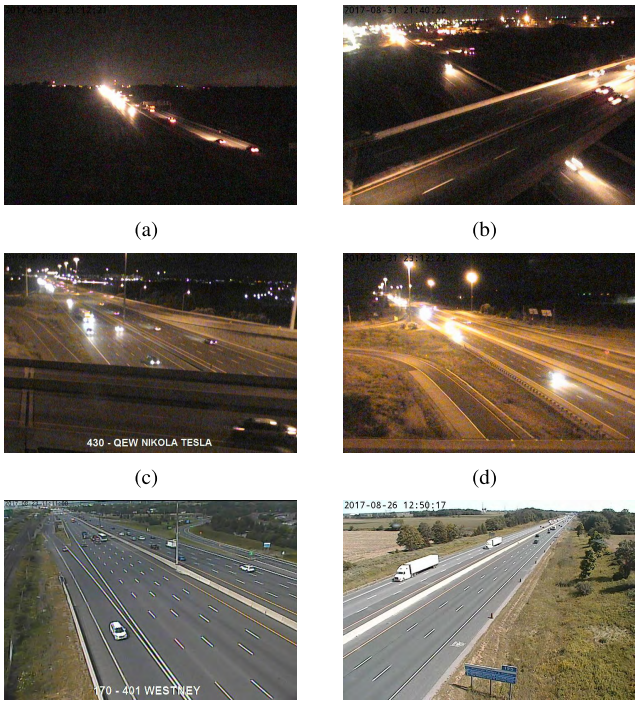

(a) (b) (c) (d) (e) (f)

FIGURE 5. Examples of training image classification, from the upper left to lower right, in Z-pattern, they are from category 1, 2, 3, 4, 5, 6 respectively.

Algorithm 2 SVM Training

1: Establish the initial image library.
a) Collect the training images.
b) Manually divide the images into six categories.
2: Extract the feature vectors (gray scale histogram **H**).
3. Set the kernel function type (linear kernel (9)).
4: Generate the multi-classifier **C**.
5: Evaluate the classifier by cross-validation.
6: **END**

The visibility using SVM (V_3) can be computed using the classifier output Ω, where $V_3 = \Omega \times 100/6$. Therefore,

Algorithm 3 Visibility Estimation using SVM

1: Generate the gray scale histogram **H**.
2: Using multi-classifier **C** to find Ω.
3: Compute visibility $V_3 = 100 \times \frac{\Omega}{6}$.
4: **END**

V_3 is a quantized value with a quantization step of ~ 16.66. Reducing the quantization step can be achieved by increasing the number of categories, however, the accuracy of V_3 may remain unchanged as the classification error may increase as well. Moreover, labeling the images with high degree of similarity might be inaccurate. The procedure for computing V_3 is given in **Algorithm 3**.

It is worth noting that V_3 might be different from the true visibility V_T perceived by human eyes or measured by instruments, which indicates that there is a lack of similar samples in the training sample library. Thus, new training images need to be added to the correct category in the library and the system needs to be re-trained.

C. COMPREHENSIVE VISIBILITY INDICATOR

Image visibility estimation using the weighted entropy and SVM can generate generally satisfactory results. However, the results of both techniques do not necessarily match, and there would be a difference between them. Therefore, a new method is presented to combine the results of the two methods to generate the final image visibility. The combined method will be denoted as the comprehensive visibility indicator V.

The direct approach for integration is to combine the two visibility values from two different techniques. If the weighted entropy result V_2 and SVM result V_3 are relatively close, the two results are considered credible and the average value of the two results is considered as the final visibility indicator. On the other hand, if the weighted entropy V_2 and SVM result V_3 differs significantly, then it is required to determine which one is likely to be the correct result according to the fog density parameter V_1, and the two results V_2 and V_3 are combined with different weights. The proposed algorithm is called Comprehensive Visibility Indicator (CVI) Algorithm, which is detailed in **Algorithm 4**. Moreover, the parameters and formulae used to generate V in **Algorithm 4** are obtained experimentally using 1000 images. The visibility estimates V_2 and V_3 are considered different when $\Delta \triangleq \frac{|V_2 - V_3|}{\max(V_2, V_3)} > 0.3$. In addition, an image is considered foggy when the fog density indicator $\bar{F}_D > 40$. Initial results for V show that for most daytime images $V > 50$, and for most night time images $V \leq 30$, regardless of the fog density. Therefore, a second iteration is required to scale the results of the first iteration while taking the fog density into consideration. In particular, the visibility of images for daytime with fog and night time without fog.

In step 11 of **Algorithm 4**, the condition is used to identify daytime image with fog, and then reduce V by subtracting a weighted $\bar{F}_D$. The condition in step 13 is used to identify night time image without fog, and then improve V by adding the weighted $\bar{F}_D$.

Algorithm 4 Comprehensive Visibility Indicator

1: **Inputs:** V_2, V_3, $\bar{F}_D$
2: Compute Δ, $V_{av} = \frac{1}{2}(V_2 + V_3)$
3: **If** $\Delta < 0.3$
4: $V = V_{av}$
5: Go to 15
6: **If** $\bar{F}_D > 40$
7: $V^{(1)} = \frac{\max(V_2, V_3)}{V_{av}} \min(V_2, V_3)$
8: **Else**
9: $V^{(1)} = \frac{1}{2V_{av}} \left((\min(V_2, V_3))^2 + (\max(V_2, V_3))^2 \right)$
10: **End**
11: **If** $\left[V^{(1)} > 50\right]$ & $\left[\bar{F}_D > 40\right]$
12: $V = V^{(1)} \left(1 - \left(\frac{\bar{F}_D}{V^{(1)}}\right)^2\right)$
13: **Elseif** $\left[V^{(1)} \leq 30\right]$ and $\left[\bar{F}_D < 20\right]$
14: $V = V^{(1)} \left(1 + \left(\frac{\bar{F}_D}{V^{(1)}}\right)^2\right)$
15: **End**
16: **END**

TABLE 1. Visibility evaluation criteria.

NVR	VL	Min (m)	Max (m)
75-100	L_4	400	∞
50-74	L_3	200	399
25-49	L_2	100	199
0-24	L_1	0	99

V. RESULTS

This section presents the results obtained using the proposed visibility algorithm. The images are real road images collected from various parts of highways in Canada and are provided by the Ministry of Transportation of Ontario (MTO). In the experiments, more than 1000 images are chosen under various driving conditions, including daytime images with good visibility, foggy, rainy, snowy and dark images with limited visibility. In order to associate the visibility indicator with real-life measured visibility, the visibility levels (VL) are defined in Table 1. Visibility distance is divided into 4 levels based on the criteria proposed in [38], because drivers observe the difference when visibility changes from good→normal, normal⟶bad, and bad→ terrible. The first column in Table 1 corresponds to the normalized visibility range (NVR), which is the visibility on a scale of [0, 100]. In this paper, four values are presented for each image based on the method used to derive the visibility, namely, fog density (V_1), entropy (V_2), SVM (V_3), and CVI (V).

To evaluate the efficiency of the proposed fDCP, the execution time of fDCP module is compared with the conventional DCP (cDCP) [35]. The two algorithms are used to process 200 images and their running time is calculated and displayed in Fig. 6. The top green line represents the execution time for

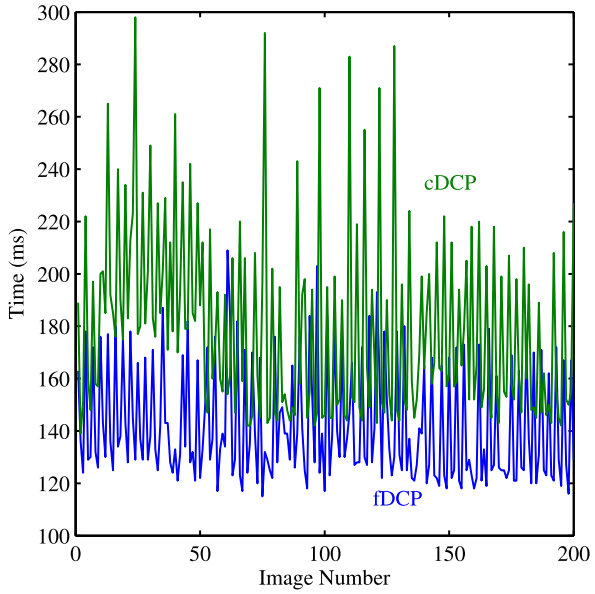

FIGURE 6. The comparison of execution time of conventional DCP and fast DCP.

cDCP and the bottom blue line represents the execution time for fDCP. It can be seen that for most images, the processing time by cDCP is higher than fDCP, with differences ranging from 5 ms to 163 ms. In addition, the average execution time of cDCP and fDCP is about 179 ms and 141 ms, respectively. Therefore, the average improvement in the execution time by the fDCP is about 26%.

To evaluate the accuracy of the fDCP visibility estimates, the fDCP results are compared with human perception results, where 40 images that represent various visibility conditions were applied to the fDCP algorithm, and then V_1 is calculated. The same 40 images were classified by 10 people, and the final level is computed as the average of the 10 human estimates rounded to the nearest integer. The obtained results show that the fDCP matches the human perception in about 42.5% of the images. Moreover, the level values using the fDCP are generally higher than the human perception, which is due to the fact that dark images are typically given high level values by the fDCP.

The SVM classifier was trained using 1000 images and tested using 5-fold cross validation. The images were chosen such that each of the six categories has roughly the same number of images. The results of the cross-validation testing process in terms of average accuracy (Avg. Acc.) are shown in Table 2. The results are presented for each of the 5 tests performed on each fold, and for each of the 4 levels. As can be noted from Table 2, L_4 has the highest accuracy, while L_1 has the lowest. Moreover, the overall classifier accuracy is 83.5%.

The results of six representative sample images from Fig. 5 are outlined in Table 3. By analyzing the obtained results in Table 3, it can be noted that V_1 is always high even in dark images. Such a result is expected because V_1 solely depends on the fog density, while all subfigures in Fig. 5 are

TABLE 2. SVM testing accuracy results using 5-fold cross-validation.

	L_1	L_2	L_3	L_4	**Avg. Acc.**
Test 1	87.0	92.3	83.3	93.1	88.9
Test 2	79.6	74.3	79.2	87.9	80.9
Test 3	77.8	95.0	89.6	82.8	85.5
Test 4	87.0	75.0	91.7	77.6	83.0
Test 5	72.7	87.5	73.5	84.5	79.2
Avg. Acc.	80.8	84.8	83.4	85.2	83.5

TABLE 3. Visibility results and the corresponding visibility levels for the images in Fig. 5.

	V_1		V_2		V_3		V	
Fig. 5a	98.2	L_4	8.1	L_1	16.7	L_1	13.9	L_1
Fig. 5b	97.6	L_4	22.5	L_1	33.0	L_2	29.0	L_2
Fig. 5c	95.4	L_4	32.9	L_2	50.0	L_3	43.2	L_2
Fig. 5d	93.8	L_4	54.1	L_3	66.7	L_3	61.0	L_3
Fig. 5e	87.9	L_4	81.1	L_4	83.3	L_4	82.2	L_4
Fig. 5f	88.0	L_4	89.5	L_4	100.0	L_4	94.7	L_4

not foggy. The visibility results obtained using V_2 and V_3 are more accurate, yet they have large difference, $\Delta > 0.3$, in 3 out of the 6 considered cases, which are gray shaded in Table 3. Therefore, the final visibility V for images in Fig. 5a, 5b and 5c has to be computed iteratively with the aide of the fog density, while in the other three subfigures the final visibility is just the average of V_1 and V_2. Moreover, the Table shows that there is noticeable discrepancy in the visibility levels computed based on the four considered techniques. In particular, the levels generated using V_1 do not match the levels obtained using the other three approaches in 4 out of the six analyzed figures. Comparing V_2 and V_3 shows that they have two differences where V_2 estimated levels are less than V_3. For the case of V, it can be noted that it does not match V_2 for Fig. 5b, and does not match V_3 for Fig. 5c, which to a certain extent agrees with the human perception of these figures.

To verify the theoretical results obtained using the CVI and other methods, several experiments were performed, where some images were collected under extreme weather conditions. For each image collected, the visibility distance (VD) was measured experimentally to allow fair comparison between the theoretical computations and measurements. In the experiments, the visibility distance is defined following [45] which defines the visibility as the greatest distance at which a black object of suitable dimensions, situated near the ground, can be seen and recognized when observed against a bright background. In the experiments, the object considered is a human body. During the experiments, two persons are involved, the first person remains in a fixed location while the second person moves straight on the road until he is not visible to the stationary person. Once the moving person is declared invisible, the first person captures the image, and the visibility distance between them is calculated using their GPS positions.

The experimental measurements of a sample of the captured foggy images shown in Fig. 7 are compared with their theoretical results in Table 4. The methods compared with

(a) (b) (c) (d) (e) (f)

FIGURE 7. Sample of the captured foggy images for the practical visibility distance measurements, their measured visibility distances are 38 m, 64 m, 73 m, 168 m, 296 m and 358 m, respectively.

TABLE 4. Visibility results of poor visibility images.

VD (m) (Measured)	**38**	**64**	**73**	**168**	**296**	**358**
VL (Measured)	L_1	L_1	L_1	L_2	L_3	L_3
VL, [38]	L_1	L_1	L_1	L_1	L_2	L_3
VL, [39]	L_4	L_1	L_3	L_3	L_3	L_3
VL, [15]	L_1	L_2	L_2	L_3	L_3	L_3
VL, CVI	L_1	L_1	L_1	L_2	L_2	L_3
NVR, CVI	24.6	14.5	22.7	39.6	39.0	55.8

the proposed method includes the conventional DCP [38], entropy [39] and artificial neural networks (ANN) [15].

In Table 4, the theoretical results that disagree with the experimental measurements are gray shaded. As can be noted from the results, the entropy method [39] has poor results while the DCP method [38] shows better performance, which can be noted from the difference between the visibility levels for the two cases. This can be explained by the fact that these images are foggy images and the DCP method calculates the visibility value based on fog density. Nevertheless, the entropy method could have better performance for other types of images like night images. The proposed system is also compared with another deep learning method [15], however, the results proved to be not convergent. We concluded that the amount of training data was not enough to get a good neural network convergence. On the other hand, SVM method shows good accuracy because SVM may produce reliable results even with small size training sample. As for the proposed CVI algorithm, because it combines DCP, entropy and SVM, it offers the best performance.

In order to evaluate the proposed CVI algorithm more comprehensively, the experimental results are judged by calculating the mean absolute error (MAE) [38], which is defined as

TABLE 5. Visibility estimation accuracy using different methods compared with measure visbility.

Methods	**fDCP**	**WIE**	**SVM**	**[38]**	**[39]**	**[15]**	**CVI**
L_1	69.3	38.7	80.8	62.7	27.8	59.0	91.1
L_2	72.7	64.7	84.8	65.7	55.6	65.7	89.9
L_3	70.1	79.6	83.4	63.5	75.5	51.5	85.1
L_4	64.8	87.9	85.2	60.7	77.9	63.1	86.9
Avg. Acc.	68.9	68.0	83.5	62.9	59.3	59.7	88.2
MAE	0.57	0.52	0.19	0.66	0.82	0.70	0.14

$$\text{MAE} = \frac{1}{N}\sum_{i=1}^{N}\left|\hat{L}_i - L_i\right| \tag{25}$$

where $\hat{L}_i$ is the estimated level, L_i is the measured level, $\{\hat{L}_i, L_i\} \in \{1, 2, 3, 4\}$, and N is the number of samples used, i.e., 1000. The relationship between the visibility levels and visibility values is shown in Table 1. The final experimental results are shown in Table 5. The results in Table 5 show that the proposed CVI algorithm has better accuracy and is more effective than the methods presented in [15], [38], and [39]. Specifically, the CVI outperforms [15], [38], and [39] by about 25.3%, 28.9% and 28.5%, respectively. Since some of the experimental images were images captured under various road conditions (daytime, dark, foggy, snowy and rainy conditions), the results show that the CVI algorithm has high accuracy in almost all conditions. In addition, all experiments show that the CVI method still provides good performance when the scale of data increases, or when the images are captured by cameras or with low-pixel resolution. Such performance can be justified by noting that the CVI is based on the pixel distribution rather than the number of pixels per image.

The visibility estimated using the images captured on various highways can be used to adjust the speed limit of the highways. However, optimum speed limit adjustment based on visibility measurement is generally difficult because there are other driving conditions that affect the speed limit. However, it is still very beneficial for the drivers to utilize visibility measurements to notify the drivers of the current visibility conditions and inform them with an advisory speed limits. Consequently, using more than 1000 images with more than 100 real driving situations, the proposed speed limit adjustments as presented in Table 6, which are in-line with the suggested speed limit adjustments in [46] and [47]. Finally, the visibility indicator and the suggested speed limit of each road are sent to the drivers and the speed limit control system takes effect. Furthermore, the proposed approach can be implemented on portable devices to provide access to meteorological visibility in real-time.

Although the obtained results confirm the efficiency of the proposed CVI under various weather and time conditions, validating the results using standard image databases is typically desirable. Towards this goal, the FROSI image database is used to test the fDCP, WIE, SVM and the CVI. The SVM was tested using 5-fold cross validation using 3500 images,

TABLE 6. Suggested speed limit adjustment by visibility.

VL	Suggested Speed Limit Adjustment
L_4	No Change
L_3	Reduce 10%
L_2	Reduce 20%
L_1	Reduce 50%

and the remaining algorithms are tested using 700 images. The obtained results show that the average accuracy of the considered algorithms is 85.1%, 76.9%, 97.7%, and 98.0% for the fDCP, WIE, SVM and CVI, respectively. As it can be noted from the results, the accuracy of all algorithms has significantly improved because all FROSI images represent simple daytime foggy scenarios.

VI. CONCLUSION

This work presented a new comprehensive visibility indicator algorithm for an ITS with adaptive speed control limits as its main functionality. The proposed visibility indicator utilizes the dark channel prior, weighted image entropy and support vector machine to generate accurate visibility estimates. The three algorithms are combined through a comprehensive decision making algorithm to produce more realistic and precise visibility indicator denoted as CVI. More than 1000 real highway images were captured and used to evaluate the reliability of the proposed system. The SVM algorithm is used to create an image library to help the system determine the visibility levels of new images. The SVM is trained using six visibility classes using images from MTO and our SVM classifier with manually created library classifies new images with an average accuracy of 83.5%. The experimental results indicated that CVI calculated by the proposed method has a high average accuracy of 88.2% for estimating visibility, which is much higher than other popular visibility measurement methods. Moreover, unlike the other considered techniques, which can only show good performance when detecting foggy visibility conditions, the proposed method can measure visibility under various driving conditions including foggy, snowy, dark conditions, etc.

ACKNOWLEDGMENT

This work was supported by the Ministry of Transportation Ontario (MTO) Highway Infrastructure Innovation Funding Program (HIIFP) under Grant 051938. The authors of this paper thank the MTO and Blackberry Inc. for their support.

REFERENCES

[1] J. Zhang, F.-Y. Wang, K. Wang, W.-H. Lin, X. Xu, and C. Chen, "Data-driven intelligent transportation systems: A survey," *IEEE Trans. Intell. Transp. Syst.*, vol. 12, no. 4, pp. 1624–1639, Dec. 2011.

[2] Y. Qiang, G. Tian, Y. Liu, and Z. Li, "Energy-efficiency models of sustainable urban transportation structure optimization," *IEEE Access*, vol. 6, pp. 18192–18199, 2018.

[3] H.-T. Wu and G.-J. Horng, "Establishing an intelligent transportation system with a network security mechanism in an Internet of vehicle environment," *IEEE Access*, vol. 5, pp. 19239–19247, 2017.

[4] O. Tayan, Y. M. Alginahi, M. N. Kabir, and A. M. Al Binali, "Analysis of a transportation system with correlated network intersections: A case study for a central urban city with high seasonal fluctuation trends," *IEEE Access*, vol. 5, pp. 7619–7635, 2017.

[5] The International Transport Forum, "Road safety annual report 2014," OECD Publishing, Paris, France, Tech. Rep. OEC D/ITF 2014, May 2014.

[6] National Highway Traffic Safety Admin., U.S. Dept. Transp., Washington, DC, USA. *Traffic Safety Facts 2012*. [Online]. Available: http://www-nrd.nhtsa.dot.gov/Pubs/812032.pdf

[7] Q. Meng and J. Lin, "The modeling and simulation of vehicle distance control based on cyber-physical system," in *Proc. 7th Joint IEEE Int. Inf. Technol. Artif. Intell. Conf.*, Chongqing, China, Dec. 2014, pp. 341–345.

[8] O. Servin, K. Boriboonsomsin, and M. Barth, "An energy and emissions impact evaluation of intelligent speed adaptation," in *Proc. IEEE Intell. Transp. Syst. Conf.*, Toronto, ON, Canada, Sep. 2006, pp. 1257–1262.

[9] J.-L. Yin, B.-H. Chen, K.-H. R. Lai, and Y. Li, "Automatic dangerous driving intensity analysis for advanced driver assistance systems from multimodal driving signals," *IEEE Sensors J.*, vol. 18, no. 12, pp. 4785–4794, Jun. 2018.

[10] B.-F. Wu, Y.-H. Chen, C.-H. Yeh, and Y.-F. Li, "Reasoning-based framework for driving safety monitoring using driving event recognition," *IEEE Trans. Intell. Transp. Syst.*, vol. 14, no. 3, pp. 1231–1241, Sep. 2013.

[11] A. Anastassov, D. Jang, and G. Giurgiu, "Driving speed profiles for autonomous vehicles," in *Proc. IEEE Conf. Intell. Veh. Symp.*, Los Angeles, CA, USA, Jun. 2017, pp. 1446–1451.

[12] T. M. Kwon, "Atmospheric visibility measurements using video cameras: Relative visibility," Dept. Elect. Comput. Eng., Univ. Minnesota Duluth, Duluth, MN, USA, Tech. Rep. CTS-04-03, Jul. 2004.

[13] T. M. Kwon, "An automatic visibility measurement system based on video cameras," Dept. Elect. Comput. Eng., Univ. Minnesota Duluth, Duluth, MN, USA, Tech. Rep. MN/RC-1998-25, Sep. 1998.

[14] T. Hagiwara, S. Fujita, and K. Kizaka, "Assessment of visibility on roads under snow conditions using digital images," *J. Illum. Eng. Inst. Jpn.*, vol. 86, p. 302, Jan. 2002.

[15] A. Giyenko, A. Palvanov, and Y. Cho, "Application of convolutional neural networks for visibility estimation of CCTV images," in *Proc. Int. Conf. Inf. Netw.*, Jan. 2018, pp. 875–879.

[16] N. Hautiere and A. Boubezoul, "Combination of roadside and in-vehicle sensors for extensive visibility range monitoring," in *Proc. 6th IEEE Int. Conf. Adv. Video Signal Based Surveill.*, Sep. 2009, pp. 388–393.

[17] R. Gallen, A. Cord, N. Hautière, É. Dumont, and D. Aubert, "Nighttime visibility analysis and estimation method in the presence of dense fog," *IEEE Trans. Intell. Transp. Syst.*, vol. 16, no. 1, pp. 310–320, Feb. 2015.

[18] N. Hautière *et al.*, "Sensing the visibility range at low cost in the SAFESPOT road-side unit," in *Proc. ITS World Congr.*, 2009, pp. 1–8.

[19] M. Huang, "Visibility and confidence estimation of an onboard-camera image for an intelligent vehicle," M.S. thesis, Dept. Elect. Comput. Eng., Wayne State Univ., Detroit, MI, USA, 2015.

[20] C. Boussard, N. Hautière, and B. d'Andréa-Novel, "Vision guided by vehicle dynamics for onboard estimation of the visibility range," *IFAC Proc. Vol.*, vol. 40, no. 15, pp. 324–329, Sep. 2007.

[21] I. Keishi, T. Masao, N. Shigeyuki, and F. Haruki, "Development and certification of a visibility-range monitor by image processing," *Ann. Glaciol.*, vol. 13, pp. 117–119, 1989.

[22] Y. C. Sun, J. J. Liaw, and C. H. Luo, "Measuring atmospheric visibility index by different high-pass operations," *Proc. Comput. Vis. Graph. Image Process.*, pp. 423–428, Aug. 2007.

[23] S. Varjo and J. Hannuksela, "Image based visibility estimation during day and night," in *Proc. Asian Conf. Comput. Vis.*, vol. 9010, Nov. 2014, pp. 277–289.

[24] S.-C. Huang, B.-H. Chen, and W.-J. Wang, "Visibility restoration of single hazy images captured in real-world weather conditions," *IEEE Trans. Circuits Syst. Video Technol.*, vol. 24, no. 10, pp. 1814–1824, Oct. 2014.

[25] S.-C. Huang, B.-H. Chen, and Y.-J. Cheng, "An efficient visibility enhancement algorithm for road scenes captured by intelligent transportation systems," *IEEE Trans. Intell. Transp. Syst.*, vol. 15, no. 5, pp. 2321–2332, Oct. 2014.

[26] F. Yuan and H. Huang, "Image haze removal via reference retrieval and scene prior," *IEEE Trans. Image Process.*, vol. 27, no. 9, pp. 4395–4409, Sep. 2018.

[27] B.-H. Chen, S.-C. Huang, and J. H. Ye, "Hazy image restoration by bi-histogram modification," *ACM Trans. Intell. Syst. Technol.*, vol. 6, no. 4, 2015, Art. no. 50.

[28] B.-H. Chen and S.-C. Huang, "An advanced visibility restoration algorithm for single hazy images," *ACM Trans. Multimedia Comput. Commun. Appl.*, vol. 11, no. 4, 2015, Art. no. 53.

[29] B.-H. Chen, S.-C. Huang, C.-Y. Li, and S.-Y. Kuo, "Haze removal using radial basis function networks for visibility restoration applications," *IEEE Trans. Neural Netw. Learn. Syst.*, vol. 29, no. 8, pp. 3828–3838, Aug. 2018.
[30] B. Cai, X. Xu, K. Jia, C. Qing, and D. Tao, "DehazeNet: An end-to-end system for single image haze removal," *IEEE Trans. Image Process.*, vol. 25, no. 11, pp. 5187–5198, Nov. 2016.
[31] J.-L. Yin, B.-H. Chen, and Y. Li, "Highly accurate image reconstruction for multimodal noise suppression using semisupervised learning on big data," *IEEE Trans. Multimedia*, vol. 20, no. 11, pp. 3045–3056, Nov. 2018.
[32] K. Zhang, W. Zuo, Y. Chen, D. Meng, and L. Zhang, "Beyond a Gaussian Denoiser: Residual learning of deep CNN for image denoising," *IEEE Trans. Image Process.*, vol. 26, no. 7, pp. 3142–3155, Jul. 2017.
[33] B.-H. Chen, S.-C. Huang, and S.-Y. Kuo, "Error-optimized sparse representation for single image rain removal," *IEEE Trans. Ind. Electron.*, vol. 64, no. 8, pp. 6573–6581, Aug. 2017.
[34] X. Fu, J. Huang, X. Ding, Y. Liao, and J. Paisley, "Clearing the skies: A deep network architecture for single-image rain removal," *IEEE Trans. Image Process.*, vol. 26, no. 6, pp. 2944–2956, Jun. 2017.
[35] K. He, J. Sun, and X. Tang, "Single image haze removal using dark channel prior," *IEEE Trans. Pattern Anal. Mach. Intell.*, vol. 33, no. 12, pp. 2341–2353, Dec. 2011.
[36] A. Al-Dweik, M. Mayhew, R. Muresan, S. M. Ali, and A. Shami, "Using technology to make roads safer: Adaptive speed limits for an intelligent transportation system," *IEEE Veh. Technol. Mag.*, vol. 12, no. 1, pp. 39–47, Mar. 2017.
[37] A. Al-Dweik, R. Muresan, M. Mayhew, and M. Lieberman, "IoT-based multifunctional scalable real-time enhanced road side unit for intelligent transportation systems," in *Proc. IEEE CCECE Conf.*, Apr./May 2017, pp. 1–6.
[38] W. Xiang, J. Xiao, C. Wang, and Y. Liu, "A new model for daytime visibility index estimation fused average sobel gradient and dark channel ratio," in *Proc. IEEE Int. Conf. Comput. Sci. Netw. Technol.*, Oct. 2014, pp. 109–112, .
[39] H. Deng, X. Sun, M. Liu, C. Ye, and X. Zhou, "Infrared small-target detection using multiscale gray difference weighted image entropy," *IEEE Trans. Aerosp. Electron. Syst.*, vol. 52, no. 1, pp. 60–72, Feb. 2016.
[40] Z. Hou and W.-Y. Yau, "Visible entropy: A measure for image visibility," in *Proc. 20th IEEE Int. Conf. Pattern Recognit.*, Aug. 2010, pp. 4448–4451.
[41] C. Cortes and V. Vapnik, "Support-vector networks," *Mach. Learn.*, vol. 20, no. 3, pp. 273–297, 1995.
[42] A. Levin, D. Lischinski, and Y. Weiss, "A closed-form solution to natural image matting," *IEEE Trans. Pattern Anal. Mach. Intell.*, vol. 30, no. 2, pp. 228–242, Feb. 2008.
[43] J. Weston and C. Watkins, "Support vector machines for multi-class pattern recognition," in *Proc. Eur. Symp. Artif. Neural Netw.*, vol. 17, 1999, pp. 219–224.
[44] P. Viola and M. J. Jones, "Robust real-time object detection," *Int. J. Comput. Vis.*, vol. 57, no. 2, pp. 137–154, 2001.
[45] *Meteorological Service for International Air Navigation*, 16th ed., Int. Civil Aviation Org. Standards Recommended Pract., Annex 3, Montreal, QC, Canada, Jul. 2007.
[46] D. Xiao, Y. Fang, Y. Zhang, and Z. Guo, "Analysis of driving behavior at the bridge-tunnel transition section in reduced visibility situations," in *Proc. 4th Int. Conf. Transp. Inf. Saf.*, Aug. 2017, pp. 581–588.
[47] Y. Chen, J. Lei, W. Cheng, L. Su, and Y. Liu, "Density difference-based variable speed limit control for expressways under rainfall conditions," in *Proc. 12th World Congr. Intell. Control Automat. (WCICA)*, Jun. 2016, pp. 2913–2917.

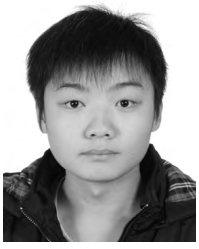

LI YANG (S'17) received the B.E. degree in computer science from the Wuhan University of Science and Technology, Wuhan, China, in 2016, and the M.A.Sc. degree in engineering from the University of Guelph, Guelph, Canada, 2018. He is currently pursuing the Ph.D. degree with the Department of Electrical and Computer Engineering, Western University, London, Canada. His research interests include intelligent transportation systems, image processing, machine learning, deep learning, cyber security, and data analytics.

RADU MURESAN received the M.A.Sc. and Ph.D. degrees in electrical and computer engineering from the University of Waterloo, Canada, in 2001 and 2003, respectively. He is currently an Associate Professor with the School of Engineering, University of Guelph, Guelph, ON, Canada. His main research interests include real-time embedded systems design, low-power wireless devices and sensing, power modeling, and system-on-chip side-channel attack countermeasure circuits for cryptographic devices. He is an Ontario P.Eng. and a member of the IEEE Circuits and System Society, the IEEE Solid-State Circuits Society, and ACM organizations.

ARAFAT AL-DWEIK (S'97–M'01–SM'04) received the B.Sc. degree in telecommunication engineering from Yarmouk University, Jordan, in 1994, and the M.S. *(summa cum laude)* and Ph.D. *(magna cum laude)* degrees in electrical engineering from Cleveland State University, Cleveland, OH, USA, in 1998 and 2001, respectively. He was with Efficient Channel Coding, Inc., Cleveland, OH, USA, from 1999 to 2001, where he was a Research and Development Engineer working on advanced modulation, coding, and synchronization techniques. From 2001 to 2003, he was the Head of the Department of Information Technology, Arab American University in Palestine. From 2003 to 2012, he was with the Communications Engineering Department, Khalifa University, United Arab Emirates. He joined the University of Guelph, Guelph, ON, Canada, as an Associate Professor, from 2013 to 2014. He has been a Visiting Research Fellow at the School of Electrical, Electronic and Computer Engineering, Newcastle University, Newcastle upon Tyne, U.K., since 2006. He is also a Research Professor and a member of the School of Graduate Studies, Western University, London, ON, Canada. He has authored over 110 published papers and five issued U.S. patents. He has extensive editorial experience, where he serves as an Associate Editor at the IEEE TRANSACTIONS ON VEHICULAR TECHNOLOGY and *IET Communications*. He has received several research awards and he was a recipient of the Fulbright Scholarship.

LEONTIOS J. HADJILEONTIADIS (S'87–M'98–SM'11) was born in Kastoria, Greece, in 1966. He received the Diploma degree in electrical engineering, the Ph.D. degree in electrical and computer engineering, and the Diploma degree in musicology from the Aristotle University of Thessaloniki (AUTH), Thessaloniki, Greece, in 1989, 1997, and 2011, respectively, and the Ph.D. degree in music composition from the University of York, York, U.K., in 2004. His publication record includes over 100 papers in peer-reviewed international journals, over 150 papers in peer-reviewed international conference proceedings, six books, two books edited, 24 book chapters, and three patents [h-index=34 (Google scholar), 28 (Scopus)]. He has a vast experience in project management, coordinating so far European projects of over US$6.000.000. His research interests include advanced signal processing, machine learning, biomedical engineering, affective computing, and active and healthy ageing. He has been awarded, amongst other awards, as an Innovative Researcher and Champion Faculty from Microsoft, USA, in 2012, and the Silver Award in Teaching Delivery at the Reimagine Education Awards from 2017 to 2018.